Atmos. Meas. Tech. Discuss., 5, 2449–2486, 2012
www.atmos-meas-tech-discuss.net/5/2449/2012/
doi:10.5194/amtd-5-2449-2012

Atmospheric Measurement Techniques Discussions

High resolution NO_2 remote sensing from the Airborne Prism EXperiment (APEX) imaging spectrometer

C. Popp[1], D. Brunner[1], A. Damm[2], M. Van Roozendael[3], C. Fayt[3], and B. Buchmann[1]

[1]Empa, Swiss Federal Laboratories for Materials Science and Technology, 8600 Dübendorf, Switzerland
[2]Remote Sensing Laboratories, University of Zurich, Winterthurerstrasse 190, 8057 Zurich, Switzerland
[3]Belgian Insitute for Space Aeronomy (BIRA-IASB), Avenue Circulaire 3, 1180 Brussels, Belgium

Received: 1 March 2012 – Accepted: 19 March 2012 – Published: 28 March 2012

Correspondence to: C. Popp (christoph.popp@empa.ch)

Published by Copernicus Publications on behalf of the European Geosciences Union.

Abstract

We present and evaluate the retrieval of high spatial resolution maps of NO_2 vertical column densities (VCD) from the Airborne Prism EXperiment (APEX) imaging spectrometer. APEX is a novel instrument providing airborne measurements of unique spectral and spatial resolution and coverage as well as high signal stability. In this study, we use spectrometer data acquired over Zurich, Switzerland, in the morning and late afternoon during a flight campaign on a cloud-free summer day in June 2010. NO_2 VCD are derived with a two-step approach usually applied to satellite NO_2 retrievals, i.e. a DOAS analysis followed by air mass factor calculations based on radiative transfer computations.

Our analysis demonstrates that APEX is clearly sensitive to NO_2 VCD above typical European tropospheric background abundances ($>1 \times 10^{15}$ molec cm^{-2}). The two-dimensional maps of NO_2 VCD reveal a very plausible spatial distribution with strong gradients around major NO_x sources (e.g. Zurich airport, waste incinerator, motorways) and low NO_2 in remote areas. The morning overflights resulted in generally higher NO_2 VCD and a more distinct pattern than the afternoon overflights which can be attributed to the meteorological conditions prevailing during that day (development of the boundary layer and increased wind speed in the afternoon) as well as to photochemical loss of NO_2. The remotely sensed NO_2 VCD are also highly correlated with ground-based in-situ measurements from local and national air quality networks ($R = 0.73$). Airborne NO_2 remote sensing using APEX will be valuable to detect NO_2 emission sources, to provide input for NO_2 emission modeling, and to establish links between in-situ measurements, air quality models, and satellite NO_2 products.

1 Introduction

Nitrogen dioxide (NO_2) is an important reactive trace gas in the troposphere. NO_2 acts as an ozone and aerosol precursor and can directly or indirectly affect human

AMTD
5, 2449–2486, 2012

health (e.g. pulmonary or cardiovascular diseases) (Brunekreef and Holgate, 2002) and ecosystem functions and services (e.g. damage of leaves, reduction of crop production, acidification) (Bell and Treshow, 2002). Besides natural sources such as lightning and soil emissions the major fraction of tropospheric NO_2 is related to anthropogenic activities, notably fossil fuel combustion by traffic and industry. Despite significant improvements of air quality in European countries during the past two decades, air quality thresholds are still frequently exceeded and further efforts are needed particularly regarding reductions of particulate matter, ozone, and nitrogen oxides ($NO_x = NO + NO_2$). Measurements of NO_2 in the troposphere are performed with various in-situ, airborne, and spaceborne instruments. Tropospheric vertical column densities (TVCD) retrieved from satellites (e.g. from the Scanning Imaging Absorption Spectrometer for Atmospheric Chartography (SCIAMACHY), the Global Ozone Monitoring Experiment (GOME(-2)), or the Ozone Monitoring Instrument (OMI)) have largely contributed to a better understanding of the global distribution of NO_2 as well as its sources and trends (e.g. Boersma et al., 2004; Richter et al., 2005; van der A et al., 2008; Zhou et al., 2012). The spatial resolution of satellite products in the order of multiple tens of kilometers is only sufficient to detect aggregate sources like entire cities (Beirle et al., 2011) and individual sources like emissions from power plants (Kim et al., 2006) or ships (Beirle et al., 2004) if they are sufficiently separated in space from other sources. Ground-based in-situ instruments, on the other hand, provide accurate and continuous trace gas measurements but lack of homogeneous geographical coverage. Airborne remote sensing observations can in this regard provide a valuable link between ground-based and spaceborne NO_2 information. For example, airborne multi-axis differential optical absorption spectroscopy (AMAXDOAS) was used to retrieve NO_2 TVCD (Wang et al., 2005), NO_2 profile information (Bruns et al., 2006), or to validate SCIAMACHY NO_2 TVCD (Heue et al., 2005). Heue et al. (2008) demonstrated the capability of an imaging DOAS instrument to retrieve two dimensional NO_2 distributions over the highly polluted Highveld plateau in South Africa.

AMTD
5, 2449–2486, 2012

The Airborne Prism EXperiment (APEX) imaging spectrometer is a state-of-the art instrument with an unprecedented combination of high spectral and spatial resolution, good two dimensional geographical coverage, and high signal stability. Two NO_2 distribution maps were retrieved from imaging spectrometer data acquired over Zurich, Switzerland, in the morning and the late afternoon of 26 June 2010. Our results are considered as one of the first spatio-temporal investigations of the NO_2 distribution on a regional to local scale. In particular, we present the first high resolution maps of NO_2 VCD in a city measured by an airborne imaging spectrometer. The specific objectives of this study are (i) the presentation of a retrieval scheme to obtain NO_2 quantities from APEX imaging spectrometry data and (ii) the qualitative and quantitative assessment of the NO_2 products, considering amongst others in-situ measurements of NO_2.

2 Instrument and data acquisition

2.1 The APEX instrument

APEX is a dispersive pushbroom imaging spectrometer for environmental monitoring developed by a Swiss-Belgium consortium in the framework of the ESA-PRODEX programme (Itten et al., 2008). APEX consists of the imaging spectrometer itself, a Calibration Home Base (CHB) for instrument calibration, and a data Processing and Archiving Facility (PAF) for operational product generation (Jehle et al., 2010). Table 1 gives a brief overview of the sensor characteristics.

The APEX imaging spectrometer consists of a CCD detector for the visible and near infrared (VNIR) and a CMOS detector for the shortwave infrared (SWIR) wavelength region. The NO_2 retrieval is based on absorption bands in the UV/VIS spectral domain and, hence, only the VNIR specification is discussed hereinafter. Since atmospheric trace gases exhibit spectrally narrow absorption features, the (spectrally) unbinned configuration was applied to provide highest spectral resolution. The spectral sampling interval (SSI) and the full width half maximum (FWHM) are non-linear functions of

AMTD
5, 2449–2486, 2012

the wavelength and increase with longer wavelengths. According to pre-flight sensor calibration, the SSI increases from 0.63 to 1.44 nm and the FWHM from 0.83 to 1.66 between 420 nm and 520 nm where NO_2 slant column densities (SCD) are usually derived. APEX is a pushbroom scanner and measures radiances in 1000 spatial pixels across-track. The extent of the flight line along-track depends on the pre-defined flight pattern. The spatial resolution in across-track direction is determined by the sensor's instantaneous field of view (IFOV) of 0.028°. The spatial resolution along-track depends on the integration time. This unparalleled combination of high resolution, geographical coverage, and high signal stability makes APEX very attractive for a range of remote sensing applications, e.g. in the fields of vegetation, atmosphere, limnology, geology, or natural hazard studies.

2.2 Test site and data

Within the APEX acceptance flight campaign in 2010, extensive data acquisition activities took place over Belgium and Switzerland. Six of these image data sets were acquired in unbinned mode over Zurich, Switzerland, on Saturday 26 June (c.f. Fig. 1). Three of them were flown around 10:00 local time (08:00 UTC) and three in the late afternoon around 17:30 local time (15:30 UTC). The data was acquired approximately 5000 m above ground with an integration time of 57 ms, leading to a pixel size of about 2.5 m across-track and approximately 6 m along-track, respectively. The entire day was cloud-free.

Zurich is Switzerland's largest city with nearly 400 000 inhabitants surrounded by an agglomeration of more than one million inhabitants. The test site includes a wide range of surface types like buildings, roads, parks, forests, and part of Lake Zurich (Fig. 1, c.f. also APEX true color composite in Fig. 7a). It also includes more rural areas with decreased atmospheric pollution levels like the Uetliberg mountain range. Several major NO_x sources were covered. Three national motorways surround the city to the north, west and south (A1, A3, A4) and major transit roads lead through the city with a usually high traffic volume. In addition, two waste incinerators as well as part

AMTD
5, 2449–2486, 2012

of the approach corridor of Zurich airport are located in the test site area. Zurich was also selected for the flight experiments because of the dense ground-based air quality network with eight stations within the range covered by APEX (Fig. 1). The National Air Pollution Monitoring Network (NABEL) provides half-hourly averaged measurements of classical air pollutants like NO_2, O_3, SO_2, PM_{10} at Zurich Kaserne (urban background, situated in a park near the city center) and Duebendorf (suburban). Additional air quality measurements and meteorological parameters are available from the intercantonal network Ostluft which maintains eight sites in the area of interest from which six sites provided data for 26 June 2010: Heubeeribuehl (periphery), Wettswil Filderen (rural, close to motorway), Wettswil Weieracher (rural), Stampfenbach (urban, kerbside, moderate traffic), Schimmelstrasse (urban kerbside, high traffic volume), and Opfikon (kerbside, motorway).

2.3 Data preparation

APEX data were acquired in unbinned mode to provide highest spectral resolution. This instrumental setting, however, is at the expense of the signal stability. To increase the signal-to-noise (SNR) ratio, the imaging spectrometer data were spatially aggregated. A box size of 20 × 20 pixels was applied which is expected to increase the SNR twenty times (or $\sqrt{400}$) assuming uncorrelated noise. An image based SNR estimation applied on the original unbinned APEX data revealed a SNR of 158.5 at 490 nm for dark surfaces (water). Spatial aggregation, hence, increases the SNR to approximately 3170 for dark surfaces. It is relevant to note that image based SNR estimates usually overestimate noise or underestimate the SNR respectively, as surface variability is inherent in the image statistics. The spatial averaging resulted in a decreased pixel size of around $50 \times 120\,m^2$.

The APEX spectrometer is spectrally and radiometrically calibrated pre-flight. However, it is worth mentioning that this calibration does not compensate for certain effects occurring in-flight. For example, pushbroom sensors are typically affected by slight spectral miss-registrations across-track, e.g spectral smile effects (D'Odorico et al.,

AMTD
5, 2449–2486, 2012

2010) which may depend on the specific flight conditions. In order to minimize these effects, the NO_2 retrieval was performed on geometrically uncorrected data to allow a scan-raw wise processing of the data. In addition, NO_2 is determined from raw data (digital numbers or DN) and a spectral calibration is performed directly as part of the retrieval algorithm to account for spectral effects under flight conditions (c.f. Sect. 3.1).

In order to obtain surface reflectance as an important input parameter of the retrieval algorithm a software binning was applied to transform the unbinned data to the standard binning pattern and the data were subsequently calibrated to at-sensor radiance using the APEX-PAF. The re-binned radiance data were then atmospherically corrected using the ACTOR-4 software tool (Richter and Schläpfer, 2002) to obtain Hemispherical-Conical-Reflectance (HCRF) data. In a last step, the unbinned and binned APEX data were geometrically corrected using the PARGE orthorectification software (Schläpfer and Richter, 2002). This processing step is needed to re-project auxiliary data (e.g. a digital elevation model (DHM25, http://www.swisstopo.admin.ch/internet/swisstopo/en/home/products/height/dhm25.html, last access: 12 March 2012)) to the raw geometry of the APEX data to allow a scan-raw wise processing as mentioned before. Further, the geocorrected data is essential to relate the APEX NO_2 vertical column density (VCD) to the in-situ measurements of NO_2 concentrations and to identify objects of interest like large NO_x point sources.

3 NO_2 retrieval

The derivation of NO_2 maps from APEX follows the two step approach usually applied to satellite NO_2 retrievals. In a first step, differential slant column densities (dSCD) are derived by the well known differential optical absorption spectroscopy (DOAS) technique (Platt and Stutz, 2008). Subsequently, the dSCD are converted to VCD by means of air mass factors (AMF) calculated with a radiative transfer model. Detailed information about the physical principles, applications, and accuracies of DOAS and AMF computations can be found elsewhere (Palmer et al., 2001; Boersma et al., 2004; Platt and Stutz, 2008).

AMTD
5, 2449–2486, 2012

3.1 DOAS analysis

Differential slant column densities (dSCD) were derived with the QDOAS software (http://uv-vis.aeronomie.be/software/QDOAS/, last access: 12 March 2012, Fayt et al., 2011). DOAS analysis requires reference spectra which we obtained from the imaging spectrometer data themselves. Reference spectra were selected for each individual (aggregated) flight column (along-track) to account for and minimize errors in the DOAS analysis due to spectral miss-calibration (e.g. spectral smile). For this purpose, ten (across-track) rows were chosen by visual inspection in a forested and elevated area to the south of the city (c.f. Fig. 7a) which is assumed to only contain a background abundance of NO_2 (pollution free). Subsequently, the ten rows were averaged in the columnar direction to increase the SNR of the reference spectra. This finally resulted in 50 across-track reference spectra per flight.

NO_2 absorption cross sections (at 293 K, Voigt et al., 2002) were subsequently fitted to the differential optical depth derived from the APEX measurements and the reference spectra. Spectrally slowly varying signatures (e.g. from aerosols or surface reflectance) were accounted for by including a fifth-order polynomial in the fit and instrumental effects such as dark current and/or straylight are dealt with in QDOAS by introducing an offset spectrum. Inelastic Raman scattering was considered by a Ring cross section computed by QDOAS (c.f. Fayt et al., 2011) and the interference with O_2-O_2 was accounted for by fitting an appropriate absorption cross section (Hermans et al., 2002). Smallest fitting errors were found by using the 470–510 nm wavelength region (c.f. red rectangle in Fig. 2). The usage of a window at shorter wavelengths (e.g. 420–470 nm) lead to increased fitting errors, probably due to the lower signal levels and higher noise (and therewith lower SNR).

Accurate wavelength calibration is an important prerequisite for the DOAS analysis. As indicated above, raw DN (digital number) data was used to keep the highest sensitivity of the measurements for the NO_2 retrieval. The spectral calibration was therefore performed with the QDOAS algorithm itself. A high resolution solar spectrum (Chance

AMTD
5, 2449–2486, 2012

and Kurucz, 2010) was applied to obtain spectral calibration information which was subsequently used to convolve and shift the high resolution absorption cross sections to the APEX specifications. Two exemplary (pre-processed) APEX spectra from the VNIR detector recorded over a residential and a remote vegetated area are illustrated in Fig. 2. The corresponding slant column fit of the pixel over the residential area is presented in Fig. 3 which also gives an impression of the sensor's spectral resolution. The quality of the DOAS fit depends on the spectral and radiometric characteristics of the instrument. The spectral calibration step in QDOAS disclosed some differences worth mentioning to the pre-flight reported APEX specifications (Sect. 2.1 and Table 1) in the 470–510 nm wavelength range. The DOAS analysis indicated that the individual channels are positioned roughly 0.6 nm higher than reported pre-flight and the (over wavelength) averaged across-track differences of their corrected position (spectral smile) is ~0.25 nm. This is in line with recent findings from an in-flight and scene based APEX performance assessment (D'Odorico et al., 2011). Furthermore, the QDOAS wavelength calibration and slit function characterisation points to a FWHM about double the spectral resolution measured in the laboratories at the CHB. The reasons for this discrepancy are not fully understood yet and further analysis is currently carried out. Finally, note that negative dSCD can occur when the SCD from the reference spectrum is larger than that from the fitted spectrum or due to noise.

3.2 Air mass factor calculation

The AMF expresses the ratio between slant and vertical column of a trace gas:

$$\mathrm{SCD} = \mathrm{VCD} \times \mathrm{AMF} \tag{1}$$

and is a measure of the average backscatter path through the atmosphere of the photons observed by the sensor. The AMF can be calculated as follows (Palmer et al., 2001; Boersma et al., 2004):

$$\mathrm{AMF} = \frac{\sum m_{\mathrm{L}}(\hat{b}) x_{\mathrm{a,L}}}{\sum x_{\mathrm{a,L}}} \tag{2}$$

AMTD
5, 2449–2486, 2012

where the subscript "L" denotes a specific atmospheric layer and m_L is the (box) air mass factor per layer. Besides the layer subcolumns of the a priori NO_2 profile ($x_{a,L}$), the AMF depends on forward model parameters ($\hat{b}$) such as the solar and viewing zenith and azimuth angles, surface albedo, aerosol extinction profile, and surface pressure. The box air mass factors were calculated using the Linearized Discrete Ordinate Radiative Transfer model (LIDORT, Spurr, 2008):

$$m_L = -\frac{1}{I}\frac{\partial I}{\partial \tau_L} \quad (3)$$

where I is the intensity of the backscattered radiance and τ_L the optical depth of layer "L".

With regard to radiative transfer computations, the surface albedo for every pixel was derived from re-binned and atmospherically corrected APEX data themselves for the central wavelength of the fitting window (490 nm). Surface height was taken from the digital elevation model DHM25 previously projected to the raw geometry of the individual flight lines. Surface pressure for every pixel was subsequently obtained applying the US Standard Atmosphere 1976 (http://www.pdas.com/coesa.html, last access: 12 March 2012). The a priori NO_2 profile was taken from the EURAD chemical transport simulations (http://www.eurad.uni-koeln.de/, last access: 12 March 2012) over Switzerland at $5 \times 5\,km^2$. The coarse resolution profile was subsequently scaled to the corresponding surface height of the aggregated APEX grid cell according to Zhou et al. (2009). Aerosol optical depth (AOD) at 500 nm was taken from the Aerosol Robotic Network (AERONET, Holben et al., 1998) site Laegeren which is within approximately 20 km from the city of Zurich. The AOD was converted to an extinction profile for every pixel assuming an exponential decrease with height and a scale height of two kilometers. The box air mass factors from three exemplary (aggregated) APEX pixels are depicted in Fig. 4. APEX's sensitivity toward a NO_2 signal is highest in the atmospheric layer below the aircraft (red horizontal line) and is decreasing toward the surface and toward higher atmospheric layers. Among all the above mentioned parameters, the surface albedo has the largest impact on the AMF, e.g. the bright surface

AMTD
5, 2449–2486, 2012

(albedo of 0.27) of case (c) in Fig. 4 highly increases the APEX sensitivity toward surface NO_2. This is supported by Fig. 5 which displays the computed AMF versus surface albedo from the easterly morning flight line and which emphasizes the importance of a good quality surface albedo data set in our NO_2 VCD determination.

Since we are using earthshine spectra as reference, the result of the DOAS fit are differential slant column densities ($dSCD = SCD_P\text{-}SCD_R$) which can be written as:

$$dSCD = (VCD_P \times AMF_P + SCD_{STR}) - (VCD_R \times AMF_R + SCD_{STR}) \quad (4)$$

where the subscripts "P" and "R" refer to tropospheric quantities under polluted and clean (reference) conditions, respectively. The stratospheric contribution to dSCD can reasonably be assumed to be constant for the polluted and reference spectra in our study region. Hence, the (additive) stratospheric SCD (SCD_{STR}) cancels out on the right hand side of Eq. (4) and AMF_P and AMF_R are calculated using only atmospheric levels up to the tropopause in Eq. (2). Rearranging Eq. (4) finally yields the VCD_P:

$$VCD_P = \frac{dSCD + VCD_R \times AMF_R}{AMF_P} \quad (5)$$

where the VCD_R has to be estimated. In our case we assume 1×10^{15} molec cm^{-2} which is in the range of previously reported rural/background tropospheric columns for European summer conditions from OMI data and an ensemble of regional air quality models (Huijnen et al., 2010). Note that dSCD varies primarily due to different NO_2 below the aircraft, mainly in the boundary layer where NO_2 profiles peak in contrast to the usually low concentrations in the free troposphere.

3.3 Post-processing

Missing pixels due to a failed dSCD fit were replaced with the mean NO_2 VCD value of the nearest neighbours (less than 5 % of all retrievals were affected). The resulting

AMTD
5, 2449–2486, 2012

NO_2 maps were subsequently de-striped in order to correct for artefacts introduced by parameters varying (randomly) across-track, e.g. the background VCD or remaining sensor artifacts. Assuming that the average NO_2 per scan line varies smoothly, a fifth degree polynomial was fitted to the average of each scan-line. The residuals per scan line were finally subtracted from the initially retrieved NO_2 VCD field.

4 Results

The capability of APEX to sense NO_2 and the NO_2 product itself are assessed and discussed in the following subsections. The NO_2 SCD fitting and the two-dimensional VCD distribution are analyzed in detail. Further, the APEX NO_2 maps are compared with ground-based in-situ measurements and yearly averaged modelled NO_2 immission fields.

4.1 SCD analysis

Histograms of derived NO_2 dSCD and the corresponding dSCD error are depicted in Fig. 6. Selected statistical parameters obtained by the DOAS analysis can be found in Table 2. In general, the histograms resemble a Gaussian distribution. The average dSCD for the morning flight lines is 9.2×10^{15} molec cm^{-2} ($\pm 8.31 \times 10^{15}$ molec cm^{-2}) which is about 2.5 times higher than the average dSCD of the afternoon flights (3.87×10^{15} molec cm$^{-2} \pm 5.09 \times 10^{15}$ molec cm^{-2}). The minimum dSCD is in the same order for both overflight times (-1.58×10^{16} molec cm^{-2} and -1.68×10^{16} molec cm^{-2}, respectively) whereas the maximum dSCD for the morning is almost twice the afternoon value (4.71×10^{16} molec cm^{-2} versus 2.86×10^{16} molec cm^{-2}). Several random and systematic error sources affect the APEX based dSCD fitting, e.g. instrumental noise, wavelength calibration, or temperature dependency of the absorption cross sections (Boersma et al., 2004). A detailed assessment of these error sources is beyond the scope of this study. Rather, we concentrate here on the overall

AMTD
5, 2449–2486, 2012

dSCD error. About 14 % of all retrievals lead to negative dSCDs for the morning overflight and 22 % for the afternoon overflight (Table 2). The averaged fitting error for the morning is 2.37×10^{15} molec cm^{-2} ($\pm 6.47 \times 10^{14}$ molec cm^{-2}) and for the afternoon 2.42×10^{15} molec cm^{-2} ($\pm 4.53 \times 10^{14}$ molec cm^{-2}). This corresponds to 24 % and 47 % of the respective absolute dSCD. The absolute dSCD fitting errors and their standard deviations are very similar for the morning and afternoon results. Further differences between the results obtained for the morning and afternoon overflights are discussed in more detail in the subsections below. In general, the dSCD errors do not reveal any geographical pattern (not shown) like e.g. correlation with albedo or surface type. SCD errors in the order of 0.7×10^{15} molec cm^{-2} are reported for different satellite NO_2 retrievals in the literature (Boersma et al., 2004, 2007; Valks et al., 2011; Valin et al., 2011). These lower SCD errors can be explained by the better characteristics of these sensors specifically designed for trace gas remote sensing (e.g. SSI, FWHM, SNR, fitting window at shorter wavelength with stronger NO_2 signal possible) as compared to APEX (c.f. Sect. 2.1 and Table 1).

4.2 NO_2 spatial distribution

The spatial distributions of NO_2 VCD over Zurich for the morning and afternoon overflights are depicted in Fig. 7b and c, respectively. In addition, a comparison between the morning APEX NO_2 VCD and modelled yearly averages of surface NO_2 concentrations for 2010 is presented in Fig. 8. The simulation is based on a high-resolution (100×100 m^2) emission inventory combined with a Gaussian plume dispersion model (SAEFL, 2004). Overall, APEX NO_2 VCDs are considerably higher for the morning than for the afternoon overflights. Especially the morning mosaic of the three flight lines reveals very distinct and plausible spatial NO_2 patters. Higher NO_2 VCD can be found in residential areas (specifically over the city), over motorways, and around the international airport of Zurich to the north of the scene. Interestingly, the enhanced NO_2 VCD values in the north-eastern part of the scene correspond to a large shopping area west of the motorway A4 (c.f. Fig. 1) which is known to have a large traffic volume

AMTD
5, 2449–2486, 2012

during shopping hours, especially on Saturdays. Higher NO_2 in the south-western part of the image area corresponds to a motorway junction where three motorway tunnels intersect open air. In general, the motorways as a prominent source of NO_2 do not show up as clearly in the APEX NO_2 VCD maps as in the model surface NO_2 (Fig. 8). One has to consider that these data were acquired on a Saturday where traffic reveals different characteristics than during weekdays, e.g. generally less traffic volume with more private transport, less commuter traffic, and less trucks. Lower NO_2 mainly occurs in remote and/or forested areas, e.g. at the Uetliberg mountain range to the south west of the city or the forested area just east of the airport. Further, the three different flight lines per mosaic generally superimpose well. Some disagreements, especially found between the westerly and central flight line, can presumably be attributed to varying NO_2 abundances in the across-track direction in the reference areas. Overall, the spatial NO_2 distribution and the above-mentioned NO_2 features are in good agreement with the modelled surface concentration in Fig. 8 underlying the capability of APEX to detect tropospheric NO_2. It should be kept in mind that the APEX data represent the NO_2 distribution at a given time under a specific weather situation while the model distribution is an annual mean estimate. APEX data also represent vertical below-aircraft columns whereas the model data are concentrations at the surface. A closer look at some exemplary and specific areas is given in Sect. 4.3.

In general, spatial gradients of NO_2 VCD are more pronounced for the morning, but enhanced NO_2 VCD around the airport, around the motorway junction, over the city and decreased NO_2 VCD in remote areas and over the lake are also detectable in the afternoon maps. The above mentioned differences can be assigned to at least two reasons. First, the NO_2 concentration was lower in the afternoon compared to the morning. The diurnal evolution of surface NO_2 concentrations measured at eight NABEL and Ostluft sites is plotted in Fig. 9. The values during the APEX overflights range from low ($4.1\,\mu g\,m^{-3}$) to polluted ($43.55\,\mu g\,m^{-3}$) depending on the location and time of day. All sites show a strong decrease of NO_2 during the morning hours and more or less stable concentrations in the afternoon (after about 12:00 UTC). This is in line

AMTD
5, 2449–2486, 2012

with increased chemical loss of NO_2 during the day due to the reaction of NO_2 with the hydroxyl radical. In addition, the development of the boundary layer is expected to lead to decreased surface concentrations due to enhanced vertical mixing in the afternoon which in turn would not affect the vertical columns. On average, the morning NO_2 abundance from the in-situ sites ($23.0 \pm 11.7\,\mu g\,m^{-3}$) is almost double the afternoon abundance ($12.0 \pm 7.9\,\mu g\,m^{-3}$) and the difference between the most polluted (Opfikon and Zurich Kaserne/Zurich Stampfenbachstrasse) and cleanest (Heubeeribuehl) is about 2.5 times larger in the morning ($38.0\,\mu g\,m^{-3}$) than in the afternoon ($16.6\,\mu g\,m^{-3}$). The higher APEX NO_2 VCDs during the morning are hence highly plausible and are supported by the surface measurements. In this regard, APEX derived NO_2 VCDs allow tracking part of the diurnal NO_2 cycle.

Second, it can be assumed that the NO_2 is more homogeneously mixed in the atmosphere, both vertically and horizontally, once the boundary layer is fully developed in the afternoon (~400 m during the morning and ~1600 m during the afternoon overflight according to the COSMO numerical weather forecast (Baldauf et al., 2011)). Wind speed and direction measured at two different sites maintained by the Swiss Federal Office of Meteorology and Climatology (Fig. 10) show that the meteorological situation changed distinctively shortly after the morning APEX flights, i.e. wind speed sharply increased by nearly four times until noon and the wind direction switched from northwest to northeast typical of a Bise situation. The stronger winds lead to a stronger dilution and more rapid transport of NO_2 to regions downwind of its main emission sources. This behaviour partly explains the larger NO_2 variability and therewith better detectability of NO_2 sources for the APEX sensor during the morning overflights. These meteorological conditions together with the diurnal cycle of NO_2 are also of particular interest with regard to the planning of future flight campaigns.

Finally, Different parameters related to the sensor characteristic and retrieval algorithm may also partly account for the reported differences. The selected reference spectra should ideally be determined from a pollution-free area with a high albedo and therefore high SNR. However, such ideal reference spectra could not be found in the

AMTD
5, 2449–2486, 2012

current test area. The used reference spectra over a forested area characterized by a relatively low albedo might cause a decreased dSCD fitting quality (c.f. Sect. 4.1). Further, the contrast in NO_2 between the area where the reference spectra were chosen and the other areas are rather small for the afternoon case for reasons discussed above. This reduced contrast lead to distinctively more negative dSCD derived for the afternoon (c.f. Sect. 4.1).

Forward model parameters vary during the course of the day and therewith also the AMF. The average AMF increased from 1.51 in the morning to 1.71 in the afternoon. The major part of this change can be assigned to an increase in the aerosol optical depth from 0.19 to 0.26 (at 500 nm) based on Sun photometer measurements from the nearby AERONET site Laegeren. The solar zenith angles were quite similar for the morning (at 08:00 UTC ~48.2°) and afternoon (around 15:30 UTC ~52.9°) but these differences nevertheless slightly affect to AMF. Uncertainties in AMF are known to be a major source of uncertainty in NO_2 VCD retrievals. For example, several studies (Boersma et al., 2004, 2007; Zhou et al., 2010) estimated AMF uncertainties in the range of 30 % for OMI and SCIAMACHY. A somewhat lower AMF uncertainty can be expected in the presented retrieval because we do not have to deal with cloud contamination which is an important part of the AMF uncertainty (Boersma et al., 2004; Popp et al., 2011). However, a detailed sensitivity analysis of our AMF computations is beyond the scope of this study.

4.3 Examples of source identification

A more detailed view of specific NO_2 features detected by APEX is illustrated on the basis of three examples in Fig. 11 where the yearly averaged modelled surface concentrations are plotted for comparison. The first example (Fig. 11a and b) focuses on an area around the south-eastern part of Zurich's international airport. The enhanced surface NO_2 concentrations around the end of the two runways are well captured by the APEX VCD map. These two features are most likely caused by emissions from aircraft landing and taking off. Additionally, the APEX RGB image (Fig. 11c) acquired in the

AMTD
5, 2449–2486, 2012

morning shows different aeroplanes in motion around the hangar and one at the engine test stand (encircled red) close to the area of maximum NO_2 VCD in this example. In contrast, APEX VCD does not mirror the enhanced surface NO_2 concentrations above the motorway A51 which might be explained by the different traffic characteristics on a Saturday morning. The second example (Fig. 11d and e) displays the area around the waste incinerator Hagenholz situated between the city and the airport (c.f. map in Fig. 1). The plume of the waste incinerator pointing in the southwest direction does clearly emerge in the RGB subscence (Fig. 11f). The increased NO_2 around the chimney is well detectable in the APEX VCD maps while the immission model representing surface concentrations does not reflect the emissions from this elevated source. The third example shows an area around the lower part of Lake Zurich, including the national motorway A3 and the harbor/dockyard at the shore of Lake Zurich. In general, the spatial gradients of the yearly average surface NO_2 distribution are reproduced well by APEX VCD. Also the NO_2 abundance from traffic emissions along the motorway A3 are detectable in this example. In contrast to the first example, this specific leg of the motorway A3 is located in a N-S oriented valley, which likely channeled emitted NO_2. The smeared-out patterns of NO_2 over and around the lake basin is a result of locally transported NO_2. The NO_2 hot spot in the southern part of example three is situated over the harbor/dockyard area of Zurich. The APEX RGB image (Fig. 11i) shows a vessel on the ramp of the dockyard during the morning overflight. However, if specific engine tests were performed or not is unknown.

4.4 Comparison to ground-based measurements

The APEX derived NO_2 VCD are subsequently compared to the ground-based in-situ measurements. It is relevant to note that APEX NO_2 VCD cannot be directly validated with the in-situ NO_2 concentrations since APEX NO_2 VCD is a columnar product (in molec cm^{-2}) while the in-situ measurements represent a trace gas concentration (in $\mu g\, m^{-3}$). Nevertheless, we apply this direct comparison for a qualitative evaluation.

AMTD
5, 2449–2486, 2012

The evaluation result is illustrated in Fig. 12 where the APEX retrieved NO_2 VCD is plotted as a function of the in-situ measurements at eight NABEL and Ostluft sites. In general, a good agreement between the APEX derived NO_2 VCD and in-situ concentrations can be found and the correlation coefficient is relatively high ($R = 0.73$). Boersma et al. (2009) compared OMI and SCIAMACHY TVDC with surface measurements in Israeli cities and found correlations in the order of $R = 0.64$. This clearly underlines the capability of the APEX instrument to sense spatial NO_2 gradients. The mean absolute deviation is 2.07×10^{15} molec cm^{-2} or 29 % of the mean NO_2 VCD of these match-ups. The correlation coefficient for the morning and afternoon results separately are almost identical ($R = 0.61$).

5 Conclusions

We presented the first highly detailed two-dimensional NO_2 fields derived from the airborne APEX imaging spectrometer taking advantage of its unique combination of high spectral and spatial resolution and high number of pixels. Radiance data were acquired twice over Zurich, Switzerland, in the morning (10:00 LT) and afternoon (17:30 LT) of a cloud-free summer day in June 2010. The main results and conclusions from this study can be summarized as follows.

1. Although not primarily designed to retrieve atmospheric constituents, APEX is clearly sensitive toward NO_2 above typical European background concentrations. The DOAS analysis revealed a mean dSCD of 9.2×10^{15} molec cm^{-2} and 3.9×10^{15} molec cm^{-2} for the morning and afternoon overflights with a mean fitting error of around 2.4×10^{15} molec cm^{-2} for both.

2. The results revealed very plausible spatial distributions of NO_2 VCD over the greater Zurich area, e.g. high abundances downwind of the runways of Zurich's airport, in the city, over a shopping area, or around a waste incinerator. Lowest

AMTD
5, 2449–2486, 2012

NO_2 was found in remote places like the forested hills around the greater Zurich area. APEX is thus clearly suitable to detect individual NO_2 pollution sources.

3. The NO_2 maps from the morning and afternoon overflights showed significant differences. Spatial gradients were much more pronounced in the morning which could mostly be assigned to the meteorological parameters (lower BLH and lower wind speed) and chemical loss of NO_2 due to reaction with the hydroxyl radical. Using APEX observations, it is also possible to roughly capture the diurnal cycle of atmospheric NO_2 as the morning overflights exhibited higher NO_2 than the afternoon overflights.

4. APEX NO_2 VCD were in very good agreement ($R = 0.73$) with ground-based in-situ air quality measurements from the Swiss National Air Pollution Monitoring Network (NABEL) and the inter-cantonal network Ostluft. This further underlies the good performance of APEX and the capacity to capture atmospheric NO_2 from its data.

The overall quality of the APEX retrieved NO_2 VCD to also depends on external parameters which should already be accounted for during flight planning. Preferably, APEX data should be acquired in an operation mode, which allows optimizing SNR (e.g. increased integration times). Further, pollution-free regions should be present in the imaged area in order to select appropriate reference spectra. These spectra should, if possible, be acquired over bright surfaces. Finally, the spectral calibration and slit function characterisation with QDOAS pointed to a doubling of the spectral resolution in-flight compared to pre-flight laboratory characterisation. Possible causes for this discrepancy are currently under investigation and such findings might help to optimize future instrument set-ups.

The findings of this study clearly reveal a high spatio-temporal variability of NO_2. Airborne-based NO_2 retrieval, such as presented in this study, allows detecting NO_2 emission sources, provides valuable input for NO_2 emission modeling, or helps to strengthen the link between air quality models and satellite NO_2 products. This all

AMTD
5, 2449–2486, 2012

together enables to increase the knowledge on processes and characteristics of NO_2 tropospheric distribution. Additional and complementary APEX flights have been carried out in the meantime and others are currently in planning. The growing data base of observations will be used to enhance the APEX NO_2 retrievals but also to gain knowledge on spatio-temporal NO_2 distribution.

Acknowledgements. The authors acknowledge Hyper-Swiss-Net which is jointly funded by the Swiss University Conference and the ETH Board as an Innovation/Cooperation project (Reference number C-19). We like to thank NABEL and Ostluft for providing in-situ measurements. The QDOAS team at BIRA is supported by the Belgian Science Policy, in particular through the AGACC-II and PRODEX A3C projects. We thank the APEX team for providing and coordinating the APEX flight activities and Andreas Hüni for fruitful discussions.

References

Baldauf, M., Seifert, A., Förstner, J., Majewski, D., Raschendorfer, M., and Reinhardt, T.: Operational Convective-Scale Numerical Weather Prediction with the COSMO Model: Description and Sensitivities, Mon. Weather Rev., 139, 3887–3905, doi:10.1175/MWR-D-10-05013.1, 2011. 2463

Beirle, S., Platt, U., von Glasow, R., Wenig, M., and Wagner, T.: Estimate of nitrogen oxide emissions from shipping by satellite remote sensing, Geophys. Res. Lett., 31, L18102, doi:10.1029/2004GL020312, 2004. 2451

Beirle, S., Boersma, K. F., Platt, U., Lawrence, M. G., and Wagner, T.: Megacity Emissions and Lifetimes of Nitrogen Oxides Probed from Space, Science, 333, 1737–1739, doi:10.1126/science.1207824, 2011. 2451

Bell, J. N. B. and Treshow, M.: Air Pollution and Plant Life, John Wiley & Sons Ltd., Chichester, UK, 2002. 2451

Boersma, K. F., Eskes, H. J., and Brinksma, E. J.: Error analysis for tropospheric NO_2 retrieval from space, J. Geophys. Res., 109, D04311, doi:10.1029/2003JD003962, 2004. 2451, 2455, 2457, 2460, 2461, 2464

Boersma, K. F., Eskes, H. J., Veefkind, J. P., Brinksma, E. J., van der A, R. J., Sneep, M., van den Oord, G. H. J., Levelt, P. F., Stammes, P., Gleason, J. F., and Bucsela, E. J.:

Near-real time retrieval of tropospheric NO_2 from OMI, Atmos. Chem. Phys., 7, 2103–2118, doi:10.5194/acp-7-2103-2007, 2007. 2461, 2464

Boersma, K. F., Jacob, D. J., Trainic, M., Rudich, Y., DeSmedt, I., Dirksen, R., and Eskes, H. J.: Validation of urban NO_2 concentrations and their diurnal and seasonal variations observed from the SCIAMACHY and OMI sensors using in situ surface measurements in Israeli cities, Atmos. Chem. Phys., 9, 3867–3879, doi:10.5194/acp-9-3867-2009, 2009. 2466

Brunekreef, B. and Holgate, S. T.: Air pollution and health, Lancet, 360, 1233–1242, doi:10.1016/S0140-6736(02)11274-8, 2002. 2451

Bruns, M., Buehler, S. A., Burrows, J. P., Richter, A., Rozanov, A., Wang, P., Heue, K. P., Platt, U., Pundt, I., and Wagner, T.: NO_2 Profile retrieval using airborne multi axis UV-visible skylight absorption measurements over central Europe, Atmos. Chem. Phys., 6, 3049–3058, doi:10.5194/acp-6-3049-2006, 2006. 2451

Chance, K. and Kurucz, R. L.: An improved high-resolution solar reference spectrum for Earth's atmosphere measurements in the ultraviolet, visible, and near infrared, J. Quant. Spectrosc. Ra., 111, 1289–1295, 2010. 2456

D'Odorico, P., Alberti, E., and Schaepman, M. E.: In-flight spectral performance monitoring of the Airborne Prism Experiment, Appl. Opt., 49, 3082–3091, 2010. 2454

D'Odorico, P., Guanter, L., Schaepman, M. E., and Schläpfer, D.: Performance assessment of onboard and scene-based methods for Airborne Prism Experiment spectral characterization, Appl. Opt., 50, 4755–4764, 2011. 2457

Fayt, C., De Smedt, I., Letocart, V., Merlaud, A., Pinardi, G., and Van Roozendael, M.: QDOAS Software user manual, available at: http://uv-vis.aeronomie.be/software/QDOAS/index.php (last access: 12 March 2012), 2011. 2456

Hermans, C., Vandaele, A. C., Fally, S., Carleer, M., Colin, R., Coquart, B., Jenouvrier, A., and Mérienne, M. F.: Absorption cross section of the collision-induced bands of oxygen from the UV to the NIR, in: NATO Advanced Research Workshop: Weakly Interacting Molecular Pairs: Unconventional Absorbers of Radiation in the Atmosphere, St. Petersburg, Russia, 2002. 2456

Heue, K.-P., Richter, A., Bruns, M., Burrows, J. P., v. Friedeburg, C., Platt, U., Pundt, I., Wang, P., and Wagner, T.: Validation of SCIAMACHY tropospheric NO_2-columns with AMAXDOAS measurements, Atmos. Chem. Phys., 5, 1039–1051, doi:10.5194/acp-5-1039-2005, 2005. 2451

Heue, K.-P., Wagner, T., Broccardo, S. P., Walter, D., Piketh, S. J., Ross, K. E., Beirle, S.,

AMTD
5, 2449–2486, 2012

and Platt, U.: Direct observation of two dimensional trace gas distributions with an airborne Imaging DOAS instrument, Atmos. Chem. Phys., 8, 6707–6717, doi:10.5194/acp-8-6707-2008, 2008. 2451

Huijnen, V., Eskes, H. J., Poupkou, A., Elbern, H., Boersma, K. F., Foret, G., Sofiev, M., Valdebenito, A., Flemming, J., Stein, O., Gross, A., Robertson, L., D'Isidoro, M., Kioutsioukis, I., Friese, E., Amstrup, B., Bergstrom, R., Strunk, A., Vira, J., Zyryanov, D., Maurizi, A., Melas, D., Peuch, V.-H., and Zerefos, C.: Comparison of OMI NO_2 tropospheric columns with an ensemble of global and European regional air quality models, Atmos. Chem. Phys., 10, 3273–3296, doi:10.5194/acp-10-3273-2010, 2010. 2459

Holben, B. N., Eck, T. F., Slutsker, I., Tanre, D., Buis, J. P., Setzer, A., Vermote, E., Reagan, J. A., Kaufman, Y. J., Nakajima, T., Lavenu, F., Jankowiak, I., and Smirnov, A.: AERONET – A federated instrument network and data archive for aerosol characterization, Remote Sens. Environ., 66, 1–16, 1998. 2458

Itten K.I., Dell'Endice F., Hueni A., Kneubühler M., Schläpfer D., Odermatt D., Seidel F., Huber S., Schopfer J., Kellenberger T., Bühler Y., D'Odorico P., Nieke J., Alberti E., and Meuleman K.: APEX – the Hyperspectral ESA Airborne Prism Experiment, Sensors, 8, 6235–6259, doi:10.3390/s8106235, 2008. 2452

Jehle, M., Hueni, A., Damm, A., D' Odorico, P., Kneubühler, M., Schläpfer, D., and Schaepman, M. E.: APEX – current status, performance and product generation. Proc. IEEE Sensors 2010 Conference, Waikoloa, Hawaii (USA),1–4 November 2010, CD-ROM., 2010. 2452

Kim, S.-W., Heckel, A., McKeen, S. A., Frost, G. J., Hsie, E. Y., Trainer, M. K., Richter, A., Burrows, J. P., Peckham, S. E., and Grell, G. A.: Satellite-observed US power plant NO_x emission reductions and their impact on air quality, Geophys. Res. Lett., 33, L22812, doi:10.1029/2006GL027749, 2006. 2451

Palmer, P. I., Jacob, D. J., Chance, K., Martin, R. V., Spurr, R. J. D., Kurosu, T. P., Bey, I., Yantosca, R., Fiore, A., and Li, Q. B.: Air mass factor formulation for spectroscopic measurements from satellites: Application to formaldehyde retrievals from the Global Ozone Monitoring Experiment, J. Geophys. Res., 106, 14539–14550, 2001. 2455, 2457

Platt, U. and Stutz, J.: Differential Optical Absorption Spectroscopy, Principles and Applications, Springer, Physics of Earth and Space Environments, ISBN 978-3-540-21193-8, 2008. 2455

Popp, C., Wang, P., Brunner, D., Stammes, P., Zhou, Y., and Grzegorski, M.: MERIS albedo climatology for FRESCO+ O_2 A-band cloud retrieval, Atmos. Meas. Tech., 4, 463–483, doi:10.5194/amt-4-463-2011, 2011. 2464

AMTD
5, 2449–2486, 2012

Richter, A., Burrows, J. P., Nüß, H., Granier, C., and Niemeier, U.: Increase in tropospheric nitrogen dioxide over China observed from space, Nature, 437, 129-132, doi:10.1038/nature04092, 2005. 2451

Richter, R. and Schläpfer, D.: Geo-atmospheric processing of airborne imaging spectrometry data. Part 2: atmospheric/topographic correction, Int. J. Remote Sens., 23, 2631–2649, 2002. 2455

SAEFL: Modelling of NO_2 and benzene ambient concentrations in Switzerland 2000 to 2020, Environmental Documentation No 188 Air, Berne: Swiss Agency for the Environment, Forests, and Landscape, 64 pp., 2004. 2461

Schläpfer, D. and Richter, R.: Geo-atmospheric processing of airborne imaging spectrometry data. Part 1: parametric orthorectification, Int. J. Remote Sens., 23, 2609–2630, 2002. 2455

Spurr, R.: LIDORT and VLIDORT: Linearized pseudo-spherical scalar and vector discrete ordinate radiative transfer models for use in remote sensing retrieval problems, in: Light scattering reviews, edited by: Kokhanovsky, A., Berlin, Springer, 229–271, 2008. 2458

Valks, P., Pinardi, G., Richter, A., Lambert, J.-C., Hao, N., Loyola, D., Van Roozendael, M., and Emmadi, S.: Operational total and tropospheric NO_2 column retrieval for GOME-2, Atmos. Meas. Tech., 4, 1491–1514, doi:10.5194/amt-4-1491-2011, 2011. 2461

Valin, L. C., Russell, A. R., Bucsela, E. J., Veefkind, J. P., and Cohen, R. C.: Observation of slant column NO_2 using the super-zoom mode of AURA-OMI, Atmos. Meas. Tech., 4, 1929–1935, doi:10.5194/amt-4-1929-2011, 2011. 2461

van der A, R. J., Eskes, H. J., Boersma, K. F., van Noije, T. P. C., Van Roozendael, M., De Smedt, I., Peters, D. H. M. U, and Meijer, E. W.: Trends, seasonal variability and dominant NO_x source derived from a ten year record of NO2 measured from space, J. Geophys. Res., 113, D04302, doi:10.1029/2007JD009021, 2008. 2451

Voigt, S., Orphal, J., and Burrows, J. P.: The temperature and pressure dependence of the absorption cross sections of NO_2 in the 250–800 nm region measured by Fourier-transform spectroscopy, J. Photochem. Photobiol. A., 149, 1–7, 2002. 2456

Wang, P., Richter, A., Bruns, M., Rozanov, V. V., Burrows, J. P., Heue, K.-P., Wagner, T., Pundt, I., and Platt, U.: Measurements of tropospheric NO_2 with an airborne multi-axis DOAS instrument, Atmos. Chem. Phys., 5, 337–343, doi:10.5194/acp-5-337-2005, 2005. 2451

Zhou, Y., Brunner, D., Boersma, K. F., Dirksen, R., and Wang, P.: An improved tropospheric NO_2 retrieval for OMI observations in the vicinity of mountainous terrain, Atmos. Meas. Tech., 2, 401–416, doi:10.5194/amt-2-401-2009, 2009. 2458

AMTD
5, 2449–2486, 2012

Zhou, Y., Brunner, D., Spurr, R. J. D., Boersma, K. F., Sneep, M., Popp, C., and Buchmann, B.: Accounting for surface reflectance anisotropy in satellite retrievals of tropospheric NO_2, Atmos. Meas. Tech., 3, 1185–1203, doi:10.5194/amt-3-1185-2010, 2010. 2464

Zhou, Y., Brunner, D., Hueglin, C., Henne, S., and Staehelin, J.: Changes in OMI tropospheric NO_2 columns over Europe from 2004 to 2009 and the influence of meteorological variability, Atmos. Environ, 46, 482–495, doi:10.1016/j.atmosenv.2011.09.024, 2012. 2451

AMTD

5, 2449–2486, 2012

Table 1. Selected characteristics of the APEX imaging spectrometer

	VNIR	SWIR
Spectral Range	380.5–971.7 nm	941.2–2501.5 nm
Spectral Bands	up to 334	198
Spectral Sampling Interval	0.55–8 nm	5–10 nm
Spectral Resolution (FWHM)	0.6–6.3 nm	6.2–11 nm
Spatial Pixels (across track)	1000	
Field of view	28°	
Instantaneous field of view	0.028° (~ 0.5 mrad)	
Spatial sampling interval (across track)	2.5 m at 5000 m AGL	

AMTD
5, 2449–2486, 2012

Table 2. Statistics for the NO_2 VCD retrievals from the morning and afternoon overflight (OF = overflight, Av. = average, Stddev = standard deviation). The unites are molecules cm^{-2} where not otherwise indicated.

	Av. dSCD	Stddev dSCD	Min dSCD	Max dSCD	Av. dSCD error	Stddev dSCD error	% negative dSCD
Morning OF	9.20×10^{15}	8.31×10^{15}	-1.58×10^{16}	4.71×10^{16}	2.37×10^{15} (24 %)	6.47×10^{14}	14
Afternoon OF	3.87×10^{15}	5.09×10^{15}	-1.68×10^{16}	2.86×10^{16}	2.42×10^{15} (47 %)	4.53×10^{14}	22

AMTD
5, 2449–2486, 2012

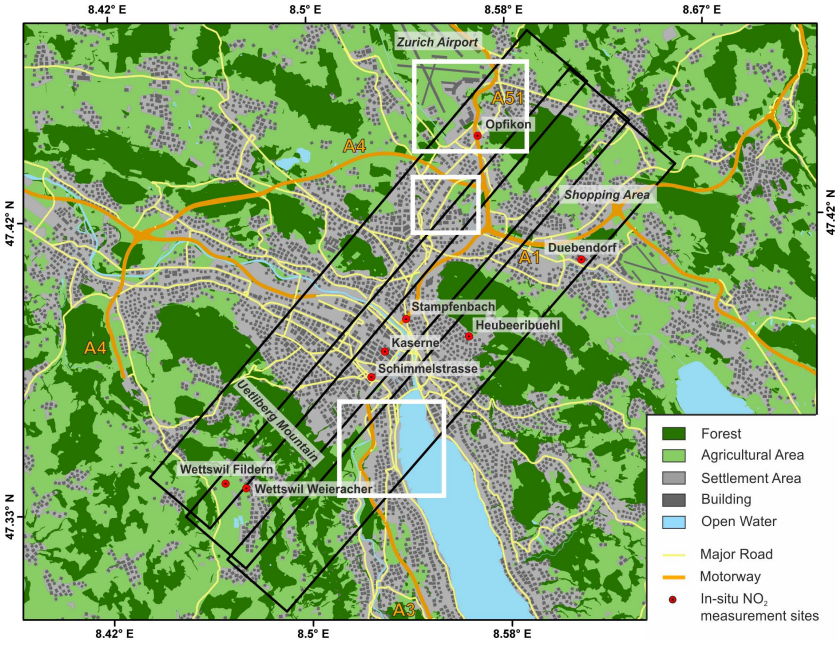

Fig. 1. Map of Zurich and surrounding areas (data source: Bundesamt für Landestopographie (Swisstopo)). The three morning flight lines are overlayed in black (the afternoon flight lines are almost identical and therefore omitted for clarity). The three white boxes correspond to the position of the examples shown in detail in Fig. 11. An APEX true color composite corresponding to this flight lines is provided in Fig. 7a.

AMTD
5, 2449–2486, 2012

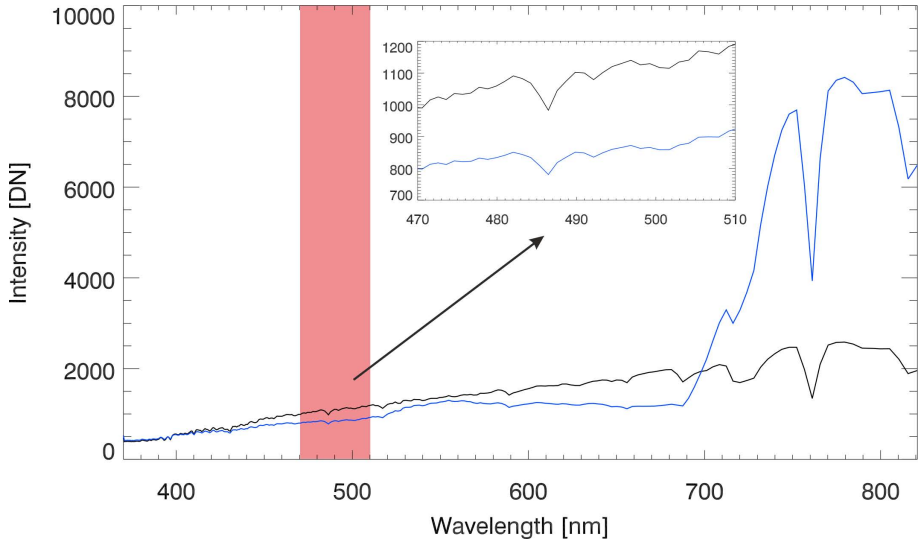

Fig. 2. Exemplary APEX spectra from the VIS/NIR detector acquired 26 June 2010 over Zurich, Switzerland. These particular spectra were recorded over a residential area in the eastern part of the city (black line) and over a remote vegetated area (blue line). The red rectangular overlay indicates the NO_2 fitting window where a zoom-in of the two spectra is also provided.

AMTD
5, 2449–2486, 2012

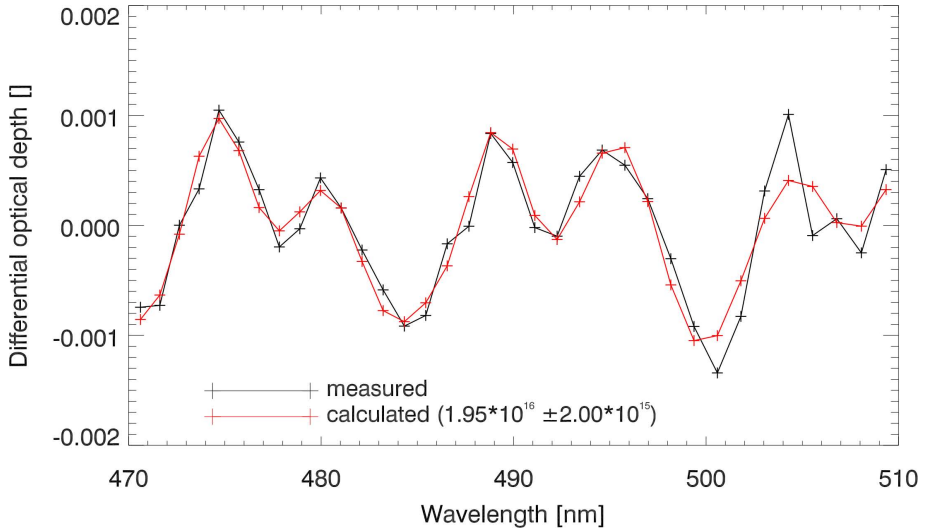

Fig. 3. Exemplary NO_2 fit for an APEX spectrum recorded over Zurich (for the pixel shown in black in Fig. 2). The RMS of the residuals of this fit is 2.61×10^{-4}.

AMTD
5, 2449–2486, 2012

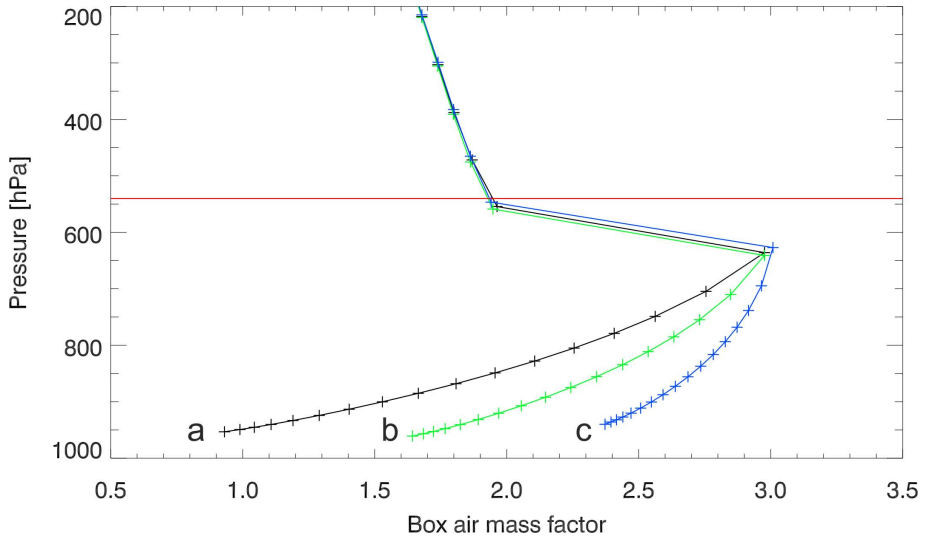

Fig. 4. Three exemplary box air mass factor curves from the APEX NO_2 VCD retrieval. Curve **(a)** represents a pixel with surface albedo (at 490 nm) of 0.05, **(b)** of 0.12, and **(c)** of 0.27 leading to AMFs of 1.46 **(a)**, 1.98 **(b)**, and 2.52 **(c)**, respectively. Note that also additional parameters such as surface pressure or observation geometry vary thereby introducing small differences between the three box air mass factor profiles. The horizontal red line depicts the flight altitude.

AMTD
5, 2449–2486, 2012

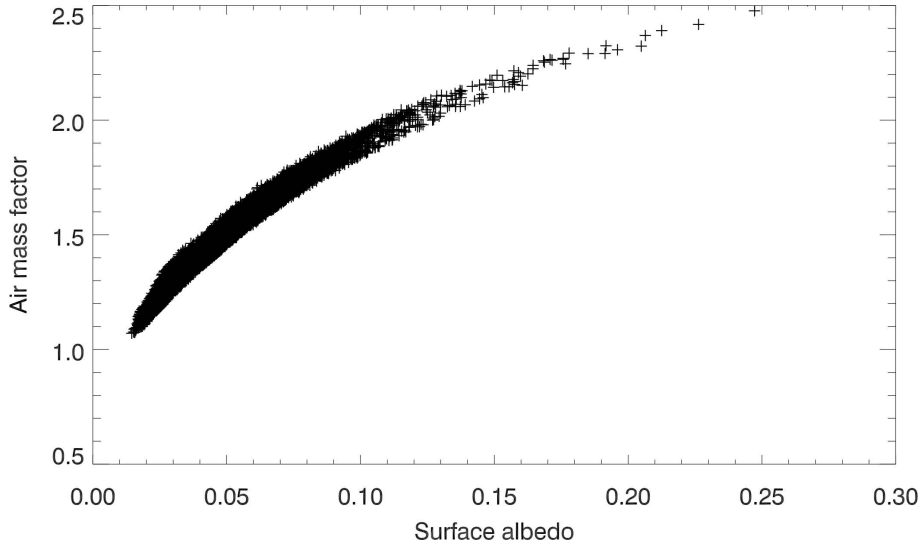

Fig. 5. Plot of the air mass factors versus their corresponding surface albedo from the easterly flight line in the morning.

AMTD
5, 2449–2486, 2012

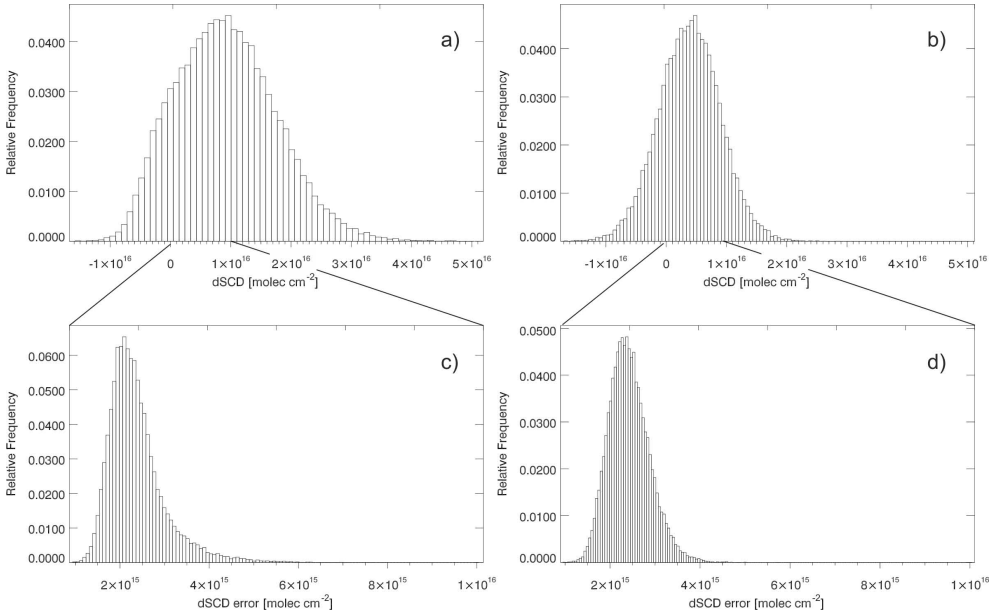

Fig. 6. Histograms of dSCD (upper panel) and dSCD errors (lower panel) for the morning (left panel) and afternoon (right panel) APEX flights. Note the much shorter scale of the x-axis in the lower panel.

AMTD
5, 2449–2486, 2012

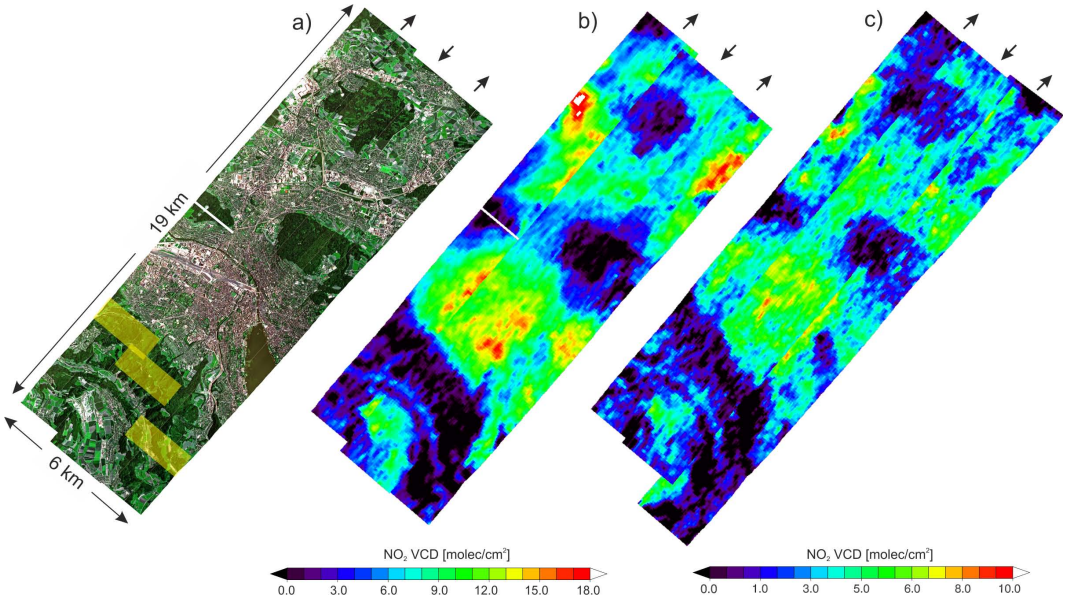

Fig. 7. RGB composite of the morning overflights **(a)** as well as retrieved NO_2 VCD from the morning **(b)** and afternoon overflights **(c)**. The morning data was recorded on 26 June 2010 around 10:00 local time (or 08:00 UTC) and the afternoon data the same day around 17:30 (or 15:30 UTC). The small arrows denote the heading of the aircraft for each flight line. The areas of each flight line where the reference spectra have been determined are denoted by the transparent yellow boxes in **(a)**. Also note the different color scale applied to **(b)** and **(c)**.

AMTD
5, 2449–2486, 2012

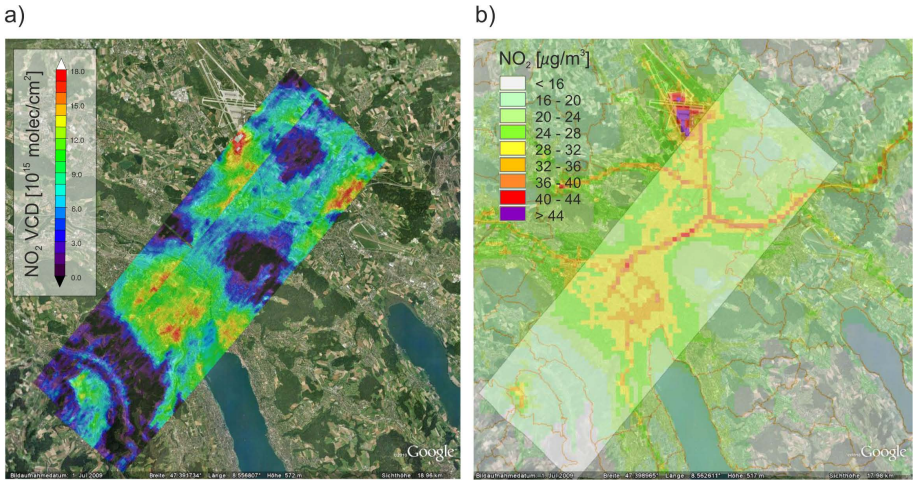

Fig. 8. Retrieved NO_2 VCD from the morning overflights over Zurich **(a)**. **(b)** illustrates the modelled yearly averages of surface NO_2 concentrations (modelled for the year 2010 and available at: http://www.gis.zh.ch/gb4/bluevari/gb.asp?app=GB-LHNO210, last access: 12 March 2012). The thin orange lines in **(b)** depict district/community boundaries.

AMTD
5, 2449–2486, 2012

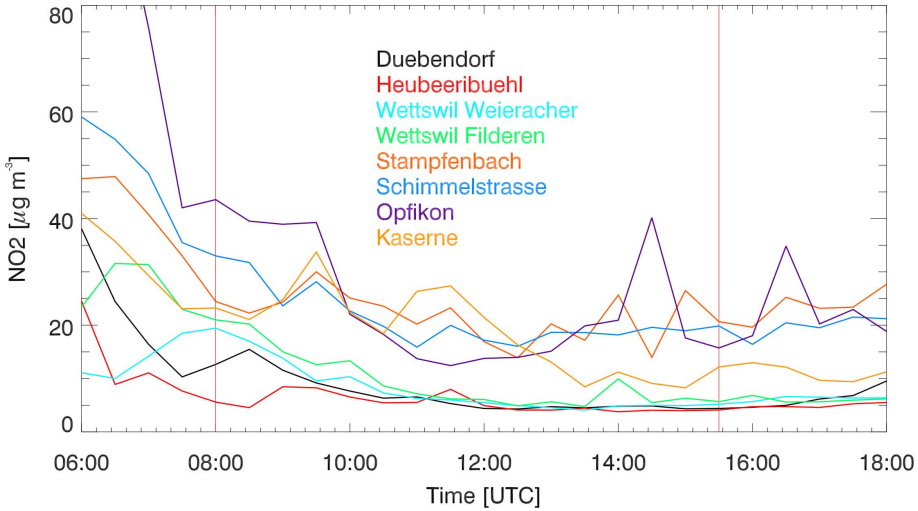

Fig. 9. Diurnal evolution of NO_2 surface concentrations at eight monitoring sites in the study region. The two vertical red lines denote the time of the APEX overflights.

AMTD
5, 2449–2486, 2012

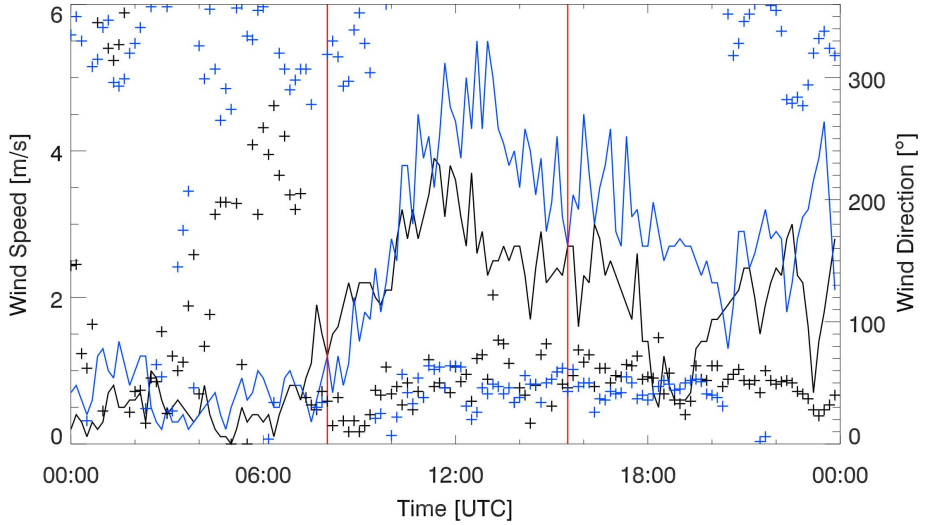

Fig. 10. Diurnal curve of wind speed (solid lines) and wind direction (crosses) at the two sites Zurich SMA (black) and Zurich Airport (blue) from measurements provided by the Swiss Federal Office of Meteorology and Climatology. The two vertical red lines denote the time of the APEX overflights.

AMTD
5, 2449–2486, 2012

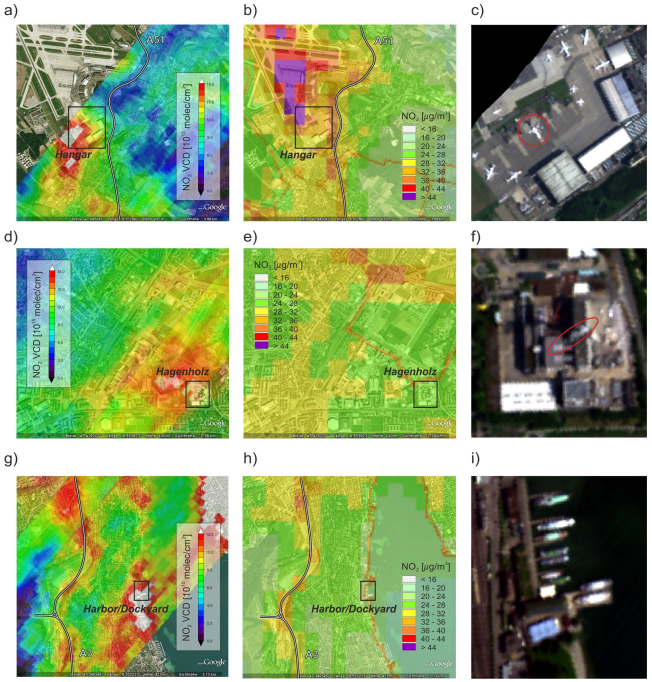

Fig. 11. Exemplary details from APEX NO_2 VCD derived from the morning overflights over Zurich (left panel) and the corresponding modelled yearly averages of surface NO_2 immissions (middle panel) for comparison (modelled for the year 2010 and available at http://www.gis.zh.ch/gb4/bluevari/gb.asp?app=GB-LHNO210, last access: 12 March 2012). The thin orange lines depict district/community boundaries. Details of the true color composite from the APEX overflight are illustrated in the right panel, i.e. aircrafts in the hangar area of Zurich airport (**(c)**, aircraft at the engine test site encircled red), plume from the waste incinerator (encircled red, **(f)**), and vessel on the ramp of the dockyard **(i)**. The outline of the three subscences are marked in the left and middle panel as the black rectangles.

AMTD
5, 2449–2486, 2012

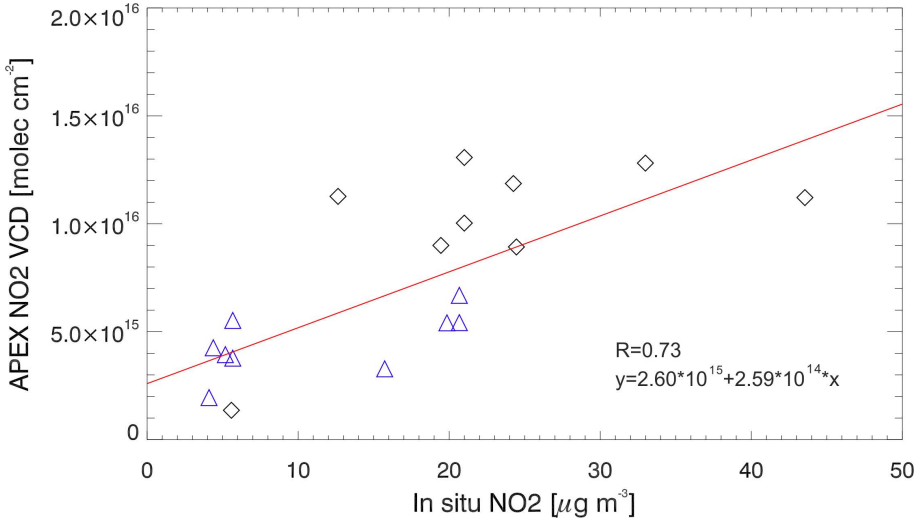

Fig. 12. Scatter plot between surface in-situ NO_2 concentrations and APEX derived VCD for the morning (black diamonds) and afternoon overflights (blue triangles). The (combined) correlation is 0.73 and the regression line $y = 2.60 \times 10^{15} + 2.59 \times 10^{14} \times x$.

AMTD
5, 2449–2486, 2012